NASA Technical Memorandum 84642

NASA-TM-84642 19830013569

DESIGN OF THE FLUTTER SUPPRESSION SYSTEM FOR DAST ARW-1R - A STATUS REPORT

JERRY R. NEWSOM, ANTHONY S. POTOTZKY,
AND IRVING ABEL

MARCH 1983

National Aeronautics and
Space Administration

Langley Research Center
Hampton, Virginia 23665

DESIGN OF THE FLUTTER SUPPRESSION SYSTEM FOR DAST ARW-1R - A STATUS REPORT

Jerry R. Newsom
NASA Langley Research Center
Hampton, Virginia

Anthony S. Pototzky
Kentron International, Inc.
Hampton, Virginia

Irving Abel
NASA Langley Research Center
Hampton, Virginia

Abstract

This paper describes the design of the flutter suppression system for a remotely-piloted research vehicle. The modeling of the aeroelastic system, the methodology used to synthesize the control law, the analytical results used to evaluate the control law performance, and ground testing of the flutter suppression system onboard the aircraft are discussed. The major emphasis is on the use of optimal control techniques employed during the synthesis of the control law.

Introduction

A considerable amount of research has been conducted in the application of active controls to increase aircraft flutter speeds. Active flutter suppression has been shown to offer significant advantages over the traditional passive means of solving flutter problems (e.g., ref. 1). To take full advantage of this technology, control law synthesis and analysis must be an integral part of aircraft design. This requires the use of synthesis methodologies and associated design aids that will enable the engineer to efficiently synthesize and analyze active flutter suppression systems (FSS). Recently, optimal control theory and optimization techniques have been demonstrated to be efficient, viable, and systematic methods for synthesizing flutter suppression control laws (refs. 2-6).

The need to experimentally validate these synthesis methods is important for general acceptance. A limited number of experimental validations have been performed (e.g., refs. 7-10). A majority of these validations have been done with wind-tunnel models. As a complement to wind-tunnel studies, flight tests are being conducted with a remotely-piloted research vehicle in a NASA program called Drones for Aerodynamic and Structural Testing (DAST; ref.11). This program involves flight testing a number of aeroelastic research wings. One of the objectives of this flight program is to evaluate the performance of active flutter suppression. This program provides an excellent opportunity to validate control law synthesis and analysis methods.

Three flight tests have been completed with the first research wing, designated ARW-1. References 12-14 describe the results of these tests. During the third flight, an error in the implementation of the FSS gain caused the system to be less stable than predicted and the vehicle encountered FSS-on flutter. Severe wing damage resulted including separation of the right wing from the aircraft. Even though the aircraft was extensively damaged, the primary components of the wing structure were salvaged and the wing has been rebuilt (now designated ARW-1R).

The purpose of this paper is to describe the overall process used to design the new flutter suppression system to be flight tested on the ARW-1R vehicle. The methodology used to synthesize the control law will be emphasized.

Nomenclature

dB	decibel
g	acceleration due to gravity
G_a	antisymmetric filter
G_c	common filter
G_s	symmetric filter
J	cost function
K_a	antisymmetric gain
K_s	symmetric gain
K_ϕ	moment arm from aircraft centerline to wing accelerometer
M	Mach number
M_{f_a}	FSS-off flutter Mach number, antisymmetric
M_{f_s}	FSS-off flutter Mach number, symmetric
q	dynamic pressure
s	Laplace variable
w_g	gust velocity
$\ddot{z}_{fus}$	fuselage acceleration, + down
$\ddot{z}_w$	wing acceleration, + down
δ	control surface deflection, + down
δ_c	actuator command
λ	eigenvalue
$\ddot{\phi}_{x_{fus}}$	fuselage roll acceleration, + right wing down
ϕ_m	phase margin
ζ_D	denominator damping ratio
ζ_N	numerator damping ratio
ω_D	denominator frequency
ω_N	numerator frequency

Matrices:

A	plant dynamics matrix
B_1	plant control distribution matrix

B_2	plant disturbance distribution matrix
C	plant output distribution matrix
K	full-state feedback gain matrix
L	Kalman estimator gain matrix
Q	output weighting matrix
R	control weighting matrix
T	similarity transformation matrix
u	actuator command vector
v	eigenvector
X	state vector
X_A	actuator state vector
X_{AC}	aircraft state vector
X_w	turbulence state vector
$\hat{X}$	estimate of state vector
Y	output vector
Z	modal coordinate vector
n_c	control process noise vector
n_g	gust disturbance noise vector
n_m	measurement noise vector

Dots over symbols denote derivatives with respect to time.

Description Of Aircraft

The general configuration of the vehicle is shown in figure 1. It is a remotely-piloted research aircraft derived from a target drone. The standard wing has been removed and replaced with an aeroelastic research wing. The vehicle is relatively small, having a wing span of 14.25 feet and a fuselage length of 27.83 feet. For the planned series of flight tests, a body conforming "belly" fuel tank is used to extend the flight test time. The wing, which has an aspect ratio of 6.8 and a supercritical airfoil shape was purposely designed to flutter within the flight envelope. A 2.2 lb. ejectible ballast is placed aft of the rear spar near each wing tip to reduce the flutter speed and to act as a "flutter stopper" upon ejection. The FSS uses four accelerometers and two control surfaces as shown in figure 1. The two accelerometers located near the control surfaces measure motions of the wing and the two in the fuselage near the c.g. are used to measure rigid-body motions. The control surfaces serve the dual functions of suppressing flutter through the FSS and of providing known excitation to the wing.

The aircraft is launched from a B-52 and recovered by a helicopter using a mid-air retrieval system. A description of the flight test technique is presented in references 11 and 12.

Structural

Modeling the structural dynamic behavior of the DAST ARW-1R vehicle has evolved over several years. The original wing finite-element model (NASTRAN) was developed by Teledyne Ryan Aeronautical (contractor for the ARW-1 wing structural design) with numerous updates from Boeing Wichita (contractor for the ARW-1 FSS design) and NASA Langley. Except for inplane motion of the wing, this model showed good correlation with the frequencies obtained from ground vibration tests (GVT). Later, the model was found to have significant shortcomings in skin cover representation and mass distributions in the wing area. During the wing rebuilding process, it was decided that a new finite-element model (ref. 15) would be developed using the Engineering Analysis Language (EAL; ref. 16). Where it was considered advantageous, the EAL model borrowed heavily from the previous NASTRAN model. Where there were shortcomings in the earlier model, EAL was used to remodel those areas. A description of the structural modeling techniques used and the rationale behind them is presented in reference 15.

The EAL model of the wing section (as shown in figure 2a) is more refined than that used in the NASTRAN model. Membrane-bending elements with laminate material properties are employed to build up both the lower and upper skin covers and the leading and trailing edge wing covers. The laminate material is represented by the anisotropic properties of fiber-oriented glass/epoxy. The closure rib and parts of the carry-through structure are modeled as isotropic plate elements. A new wing glove section has been added in the EAL model which considerably increased the inplane stiffness of the wing. The fuselage is structurally connected to the wing-carry-through-glove combination by several stiff beam ties. The wing mass distribution was closely scrutinized throughout the model development. During the rebuilding process, the mass of each component was carefully accounted for and modeled in the EAL model. As a result, the EAL model of the cantilevered wing compared quite favorably with both GVT frequencies and static deflection tests (see. ref. 15).

Aerodynamic

The generalized aerodynamic force coefficients representing the unsteady aerodynamics are computed by using the Doublet Lattice module of the Interaction of Structures, Aerodynamics, and Controls program (ref. 17). The aerodynamic coefficients for the first 10 structural modes, a control surface rotation mode, and a sinusoidal gust mode are computed. The horizontal and vertical tail surfaces are included in the computation of the overall generalized forces. The contribution of the fuselage is assumed negligible. There are a total of 222 trapezoidal boxes used to calculate the unsteady pressure distribution on all three surfaces. The box distribution (as shown in figure 2b) is most dense near the wing tip where the modeling is considered most critical and is more sparse toward the wing root. The unsteady aerodynamics are calculated for a range of reduced frequencies from 0.0 to 1.2. The reduced frequencies of open and closed loop flutter range between 0.1 and 0.16. The aerodynamics are calculated from M = 0.700 to M = 0.925 at increments of 0.025.

Flutter Suppression System Design

Methodology

A flow chart of the overall control law design process is shown in figure 3. The first element of the process is the selection of design objectives (i.e., gain margin, phase margin, etc.). The second element is the selection of a design point (i.e., Mach number and altitude). Control law synthesis is then performed at the design point using optimal control methods. Two different approaches to this key element will subsequently be described in some detail. The

next element, analysis, provides information on the performance of the control law at off-design flight conditions. If the design objectives at the off-design flight conditions are not met, then a gain scheduler which may be a function of Mach number and/or dynamic pressure is evaluated. If a gain scheduler will not meet the design objectives, then a path back to control law synthesis is selected.

In this paper, two different approaches to the optimal control law synthesis element are described. Flow charts of these two different approaches are given in figure 4. The choice of an approach usually depends on what state the overall design process is in. Generally, the modified linear quadratic Gaussian approach is used when there is no prior knowledge of a control law.

Both approaches start with the generation of a state space model. This model consists of the airplane dynamic model, actuator model, and the gust disturbance model (ref. 5) and can be expressed in equation form as:

$$\dot{X} = AX + B_1 u + B_2 n_g \qquad (1)$$

$$Y = CX + n_m$$

where

$$X = \begin{pmatrix} X_{AC} \\ X_A \\ X_w \end{pmatrix}$$

is the state vector, u is the actuator command vector, n_g is the gust disturbance noise vector Y is the output vector, and n_m is the measurement noise vector. The state space model is usually of high order. It is not unusual to have 60 or more states. For control law synthesis, it is desirable to have a model with as low an order as possible. Modal residualization (ref. 5) is used to construct a lower order "design model" for control law synthesis. The control law synthesized using this model is then analyzed using the higher order "evaluation model."

Modified Linear Quadratic Gaussian (MLQG) approach. When there is no prior knowledge of a control law definition, the MLQG approach (refs. 4 and 5) shown in figure 4a is selected. After the state space model is generated, the next step in this approach is a full-state feedback design. Full-state feedback provides for the minimization of a quadratic cost function of the output and control vectors. To find the optimal full-state feedback control law, the quadratic cost function

$$J = E[Y^T Q Y + u^T R u] \qquad (2)$$

is minimized. This leads to a control law of the form

$$u = -KX \qquad (3)$$

where K is the full-state feedback gain matrix. This control law requires that all of the state variables be fed back. Direct measurement of all state variables is not feasible. Therefore, in the next step, a Kalman estimator is used to estimate the state variables from available measurements.

Systems designed using full-state feedback have good gain and phase margins and a desirable low bandwidth. However, systems designed using a Kalman estimator can have poor gain and phase margins and an undesirable high bandwidth. To improve the stability margins during the Kalman estimator design, the input noise adjustment procedure of Doyle and Stein (ref. 18) is used. This procedure involves adding a fictitious process noise (n_c in equation 4) directly to the control input of the plant during the estimator design. In addition, varying the measurement noise intensity (n_m in equation 4) during the Kalman estimator design is used to change the bandwidth. The equations of motion are given by

$$\dot{X} = AX + B_1 u + B_1 n_c + B_2 n_g$$

$$Y = CX + n_m \qquad (4)$$

Here n_g and n_m are the disturbance and measurement noise and n_c is the fictitious process noise added at the control input. The estimator dynamics are given by

$$\hat{\dot{X}} = (A - B_1 K - LC)\hat{X} + LY \qquad (5)$$

where L is the Kalman estimator gain matrix. Derivation of the gain matrix L can be found in many texts (e.g., ref. 19). The design of the estimator involves iterating on the intensities of the fictitious process noise and the measurement noise to obtain a compromise between good stability margins, low bandwidth, and good response characteristics.

The Kalman estimator together with the full-state feedback gain matrix constitute the optimal controller. The Kalman filter and, therefore, the optimal controller will have the same order as that of the model used for the synthesis. In the case of a flexible airplane that contains a large number of structural modes, unsteady aerodynamic lag states, and actuator states the high order of the optimal controller imposes an unnecessary implementation burden. Several references (3-5) have shown that a reduced-order controller that approximates the full-order optimal controller can be found and used with little degradation in the closed-loop performance. The next two steps in this synthesis approach involve reducing the order of the optimal controller.

The transformation of the controller to block diagonal form is used to help select the states that are to be retained during the controller reduction process. A brief description of the transformation is presented in appendix A. A modal residualization technique is then used to reduce the order of the controller. The selection of the states to be retained (and thus the order) during the residualization process is based on engineering judgment.

The reduced-order controller is then analyzed with the "evaluation model" to assess its stability margins. If the margins are unacceptable, then there are two paths that can be taken. The order reduction process can be repeated with a different selection of states to be retained; or the noise intensities can be changed and the Kalman estimator design repeated. The selection of which path to take is again based on engineering judgment.

Numerical optimization approach. This approach is used when, for example, changes to the mathematical model occur and it is necessary to update a previously developed control law. The first step in this approach is to generate the state space model. The next step is the selection of design variables (coefficients of numerator and denominator polynomials) in the control law which are to be optimized.

Next, the design variables are optimized by minimizing a quadratic cost function of the same form as that used during the full-state feedback design. Gradients of the cost function with respect to design variables in the control law are determined by solving a pair of Lyapunov equations. Using the gradients, a nonlinear programing algorithm is used to search for the control law design variables that minimize the cost function. The input noise procedure previously described is used to improve the stability margins of the system.

The optimized control law is then analyzed with the "evaluation model" to examine its performance. If the design objectives are not met then there are two paths that can be taken. A different set of design variables can be selected or the noise intensities can be changed and the optimization and analysis steps repeated. The selection of which path to take is again based on engineering judgment.

Numerical Results

The first ten symmetric and antisymmetric modes, frequencies, and generalized masses from the EAL structural model are used for analysis purposes. Table 1 presents the computed frequencies of the first 10 modes. Based on the EAL model, the flutter characteristics are established and a control law is designed to provide a 10 percent increase in flutter speed. The effect of updating the EAL model (due to ground vibration tests) on the performance of the active control system is also discussed.

Basic characteristics. The predicted symmetric and antisymmetric flutter boundaries (FSS-off) are shown in figure 5. The flutter altitude shows a smooth increase with Mach number for both the symmetric and antisymmetric cases. The flutter frequencies, which are also shown in figure 5, decrease gradually with Mach number. (These flutter boundaries should not be compared to those presented in reference 13, since both the mathematical model and the wing construction have been changed.) For both the symmetric and antisymmetric cases, the critical mode is first wing bending. The antisymmetric flutter speed is approximately M = 0.09 greater than the symmetric flutter speed.

MLQG control law synthesis. The first design objective for the FSS is to provide a 10 percent increase in the minimum flutter speed (the minimum flutter speed is associated with symmetric motion) above that with the FSS-off. Flight tests are to be conducted between the altitudes of 10,000 and 20,000 feet. Therefore, 15,000 feet was arbitrarily selected to be the symmetric design point altitude. At 15,000 feet, the design Mach number was selected as M = 0.925 (1.10 x M_{f_s}). The symmetric design point (as shown in figure 5) lies very close to the antisymmetric flutter boundary. If the relative spacing between the symmetric and antisymmetric flutter boundaries is correct, the objective of demonstrating a 10 percent increase in the minimum flutter speed could be accomplished without the need for implementing an antisymmetric FSS. To protect against possible errors in this spacing, it was decided to define an antisymmetric design point and synthesize an antisymmetric FSS. The antisymmetric design point was defined in the following manner: (1) The symmetric flutter Mach number at 15,000 feet is approximately M = 0.83, (2) At M = 0.83, the antisymmetric flutter altitude is approximately 7,000 feet, (3) At 7,000 feet, the antisymmetric FSS is required to provide an increment in flutter Mach number of 0.05. Additional design objectives are that both the symmetric and antisymmetric FSS provide ± 6 dB gain margins and ± 30 degrees phase margins at speeds up to and including the 10 percent increase in the minimum flutter speed.

The state space equations are developed in the same manner as described in reference 13. The "evaluation model" contains 66 states. There are 20 structural states (10 modes), 40 aerodynamic states (4 lag states per structural mode), 4 actuator states, and 2 gust states. The actuator and Dryden gust models are given in transfer function form as:

$$\frac{\delta}{\delta_c} = \frac{1.69 \times 10^{10}}{(s^2+76.78s+87202)(s^2+589.4s+1.93\times10^5)} \qquad (6)$$

$$\frac{w_g}{\eta_g} = \frac{(1.057s+0.239)}{(s^2+0.77s+0.148)}$$

The "design model" contains 24 states. This model is developed by retaining the states associated with the first three structural modes and residualizing the states associated with the last seven structural modes. The actuator and gust states are retained in the "design model." To assess how well the "design model" approximates the "evaluation model," open-loop frequency response functions of wing acceleration due to an actuator command were compared. Figure 6 is a Bode plot of the open-loop frequency response function $\ddot{z}/\delta_c$ for both the evaluation and design models at the symmetric design condition. Both the amplitude and phase of the "design model" match the "evaluation model" well. A comparison was also performed for the antisymmetric models with similar results (not shown).

A full-state feedback control law was designed using a quadratic performance function which weights only the control input. This control law reflects the unstable poles about the imaginary axis and does not affect the other poles. It also has the property that it is the control law that stabilizes the system with the least amount of control input. A Kalman estimator was designed and combined with the full-state feedback gain matrix to generate a 24th order optimal controller. The controller was then reduced to 6th order using residualization techniques. The reduction was accomplished by retaining the states associated with the first and third structural modes and the lowest frequency actuator mode. The second structural mode was not

retained because it is primarily a fuselage bending mode. All other states were residualized. Stability analyses were then performed using the reduced-order (6th) controller with the "evaluation model" to assess the stability margins. Several iterations on the input noise and the sensor noise were required before an acceptable design was found. As the input noise was increased, the stability margins would increase but with an associated increase in the controller bandwidth. The bandwidth was decreased by increasing the sensor noise. After a tradeoff was performed between increased stability margins and controller bandwidth, the following symmetric and antisymmetric filters were synthesized.

$$G_s = K_s \frac{(s+21.33)(s^2+65.94s+18578.00)(s^2+76.78s+87202.00)}{(s^2+97.67s+3381.00)(s^2+26.00s+20938.00)(s^2+375.40s+3.58\times10^5)} \quad (7a)$$

$$G_a = K_a \frac{(s+22.10)(s^2+51.00s+18769.00)(s^2+76.78+87206.00)}{(s^2+68.41s+4419.60)(s^2+18.39s+23076.60)(s^2+278.90s+2.08\times10^5)} \quad (7b)$$

To provide good rolloff characteristics at both low and high frequencies, the following filter

$$G_c = \frac{s(1000)^2}{(s+2)(s+1000)^2} \quad (8)$$

was added to both the symmetric and antisymmetric filters. The final control laws are products of equations 7a and 8 and equations 7b and 8.

Nyquist plots for the symmetric and antisymmetric cases at their respective design points are shown in figure 7. All of the stability margin criteria are met except the positive gain margin (only +4.7 dB instead of +6dB was obtained) in the symmetric case. This violation in the positive gain margin criteria was accepted at this time for testing at subcritical velocities since it is expected that the control law will be updated prior to flight testing above the FSS-off flutter boundary.

Analysis at off-design flight conditions and gain scheduling definition. Nyquist analyses were performed at flight conditions near the respective FSS-off flutter boundaries of both the symmetric and antisymmetric cases with the control laws previously defined. The results of this analysis (not shown) indicated that both the symmetric and antisymmetric gains were too large for the system to meet the stability margin criteria. From inspection of the Nyquist plots, the values of K_s and K_a that would allow the system to meet the stability margin criteria were determined. Nyquist plots with these new values of gain are shown in figure 8. The stability margins are very good. In a similar manner, Nyquist analyses were performed at other flight conditions from M = 0.700 to M = 0.925 at increments of M = 0.025 to establish a gain schedule. These analyses indicated that the gain schedule only needed to be a function of dynamic pressure. The resulting gain schedule is given by the following equations:

$$\begin{aligned} K_s &= 110.70 && 0<q<608.40\text{psf} \\ K_s &= 110.70 + 3.06(q-608.40) && 608.40<q<720.00\text{psf} \\ K_s &= 451.70 && q>720.00\text{psf} \end{aligned} \quad (9a)$$

$$\begin{aligned} K_a &= 62.00 && 0<q<779.04\text{psf} \\ K_a &= 62.00 + 1.63(q-779.04) && 779.04<q<878.40\text{psf} \\ K_a &= 223.62 && q>878.40\text{psf} \end{aligned} \quad (9b)$$

Figure 9 shows the stability margins as a function of Mach number for both the symmetric and antisymmetric cases using the gain schedule given in equation 9. The design objectives are met except for the positive gain margin criteria in the symmetric case at M = 0.925.

To assess the effect of the control law on the higher-frequency structural modes, a gain root locus calculation was performed. Gain root locus plots are presented in figure 10 for both the symmetric and antisymmetric cases near their respective FSS-off flutter boundaries. The control law affects primarily the modes below 200 radians/second and leaves the higher frequency modes relatively unaffected as indicated by the fact that the poles for the FSS-off are essentially coincident with the poles at nominal gain.

Figure 11 shows the flutter boundaries for both the FSS-off and FSS-on cases. Both the symmetric and antisymmetric FSS-on flutter speeds are above the 10 percent increase in the minimum (symmetric) FSS-off flutter speed.

Updated structural model. As a result of a ground vibration test (GVT) of the full-up vehicle and the addition of a body conforming external fuel tank to the vehicle, the initial EAL structural model was updated. The natural frequencies, the corresponding vibration mode shapes and the structural dampings of the empty-fuel vehicle for the first three symmetric and four antisymmetric modes (ref. 15) were measured during the GVT. This information was used to update the EAL finite-element model. The update was performed by modifying the stiffness of the wing-fuselage ties, the wing-gloves, and the lateral stiffness of the fuselage. Changing the stiffness of the ties and glove areas primarily affected the first three elastic modes in both symmetries. Lowering the lateral fuselage stiffness helped lower the antisymmetric first fuselage bending frequency. Eigenvalue analyses to obtain the vibration frequencies were performed on empty, mid, and full fuel configurations. Table 2 gives the frequencies for all three fuel conditions and also shows the results of the ground vibration test frequencies of the empty vehicle.

The FSS-off flutter boundaries for the three fuel configurations are shown in figures 12a and 12b. Note that for the symmetric mid-fuel configuration the flutter boundaries for the initial EAL model and the updated EAL model differ by over 2,000 feet (the updated model indicates that the flutter boundary is at a higher Mach number and at a corresponding lower altitude). In an effort to keep the flight Mach number below M = 0.925 at the 10 percent increase in flutter speed (to minimize transonic effects), it was decided to lower the altitude for flight testing from 15,000 feet to 13,000 feet. All further calculations presented in this paper will be for an altitude of 13,000 feet. The empty fuel configuration results in the minimum symmetric flutter speed, whereas the full fuel configuration results in the minimum antisymmetric flutter speed.

Evaluation of control law with updated structural model. Stability analyses were performed using the control law defined by equations 7 and 8 and the gain schedule of equation 9 with the updated structural model. In addition, a new actuator model was also used in this analysis. The actuator model was derived from measured frequency response data of the actuators on the aircraft. A description of this data and the model will be presented in a later section of the paper. The updated structural model and the new actuator model are considered to be the best description of the aircraft dynamics prior to the first flight test.

Figure 13 shows the stability margins as a function of Mach number at 13,000 feet for both the symmetric and antisymmetric mid-fuel conditions. Analyses were also performed for the other fuel conditions but only the mid-fuel condition results are presented. For the symmetric case, the gain margins meet the design objectives except for a small violation in the negative gain margin at M = 0.925. The negative gain margin is very large near the flutter boundary (approximately -18 dB) which indicates that the gain is too large. The positive phase margins meet the design objectives up through M = 0.925. However, the negative phase margins fall short of the design objective between M = 0.85 and M = 0.89. From an inspection of the Nyquist diagrams at these Mach numbers (not shown), it was determined that the small negative phase margins are a result of the gain being too large. For the antisymmetric case, all of the stability margins meet the design objectives up through M = 0.915. However, both the negative gain margins and the negative phase margins fall short of the design objectives between M = 0.915 and M = 0.925. From an inspection of the Nyquist plot at M = 0.925 (not shown), it was determined that the gain was too small for this condition. The need for these gain changes can be attributed to changes in the flutter speed as a consequence of differences between the initial mathematical model and the updated mathematical model.

Figure 14 shows the flutter boundaries for all three of the fuel conditions. In all cases the flutter speed is increased with the FSS-on. The empty weight symmetric case has the largest increase. The full weight antisymmetric case has the smallest increase in flutter speed.

Some preliminary calculations have been performed to identify the specific changes in the control law that would be required to increase the stability margins to acceptable levels. Modification of the gain schedule (equation 9) has been identified as the simplest change. The first flight test however, will be conducted at dynamic pressures below the FSS-off flutter boundary where the proposed modification in the gain schedule has no effect. Therefore, it was decided not to modify the gain schedule before the first flight test so that data from this flight could be used to help determine if an additional update to the mathematical model (and the control law) is necessary. If such an update is necessary, then a simple modification of the gain schedule will probably not be sufficient and the numerical optimization approach previously described will be employed.

Experimental Activities

Preflight tests of both the flutter suppression system and the actuator have been completed. Figure 15 shows the block diagram of the FSS. The system configuration is identical to the previous ARW-1 system (ref. 13). The FSS is an analog system and is implemented onboard the aircraft. During the ground tests, frequency response measurements of the FSS ($G_s \times K_s \times G_c$ and $G_a \times K_a \times G_c$) were made and compared with predictions of the desired frequency response. Figure 16 shows a comparison of the measurements and the predictions. Both the gain and phase show excellent agreement.

It was required that the FSS exhibit a +6 dB gain margin on the ground. Tests were performed to establish this gain margin. These tests involved turning the FSS on and increasing the gain until either the +6 dB gain margin was reached or an instability occurred. If instabilities occur, notch filters of the form

$$\frac{s^2 + 2\zeta_N\omega_N s + \omega_N^2}{s^2 + 2\zeta_D\omega_D s + \omega_D^2}$$

are used to eliminate them. Notch filters are first implemented in the actuator loop. If this implementation does not eliminate the instability, then notch filters are implemented directly in the FSS loop. The test was performed and required the implementation of four notch filters in the actuator loop before a +6 db gain margin could be achieved. The frequencies and damping ratios for the four notch filters are listed below.

Notch	Frequency, Hz	ζ_N	ζ_D
1	125	.035	.25
2	109	.020	.25
3	142	.035	.25
4	425	.035	.25

The effect of the notch filters on the actuator frequency response is shown in figure 17. The dominant effect of the notch filters is to reduce the bandwidth of the actuator. The frequency response of the actuator with the notch filters was curve fitted to obtain the model used in the evaluation of the control law with the updated structural model. The resulting transfer function model of the actuator is given as

$$\frac{\delta}{\delta_c} = \frac{1.99\times10^{10}}{(s^2+299.40s+9.13\times10^4)(s^2+344.67s+2.46\times10^5)} \qquad (10)$$

Conclusions

The design of the flutter suppression system for a remotely-piloted research vehicle has been dicussed. As shown in this paper optimal control techniques can be used to synthesize flutter suppression control laws in a viable and systematic fashion. The design objective of increasing the minimum flutter speed by 10 percent while maintaining ±6 dB and ± 30 degrees stability margins was achieved except for a 4.7 dB gain

margin at one flight condition. This was accomplished over a wide range of flight conditions with only gain scheduling required as a function of dynamic pressure. After an update to the mathematical model, stability margins were degraded. In addition, the flutter supression system was not as effective for some off-design fuel conditions. The flutter suppression system was ground-tested and required the implementation of four notch filters in the actuator loop to eliminate high-frequency instabilities.

Appendix A

Transformation of Controller to Block Diagonal Form

Consider a similarity transformation matrix T, whose columns consist of the following vectors

$$T = [\, t_1, t_2, \ldots, t_n] \qquad (A1)$$

where the elements of the vectors t_i (i=1,n) are all real. For any real eigenvalue λ_i, the vector t_i is equal to the real eigenvector v_i. For any complex eigenvalue λ_i and its conjugate λ_{i+1}, the vectors t_i and t_{i+1} are given by

$$t_i = Re(v_i) + Im(v_i) \qquad (A2)$$

and

$$t_{i+1} = Re(v_i) - Im(v_i) \qquad (A3)$$

where $Re(v_i)$ and $Im(v_i)$ denote respectively the real and imaginary parts of the complex eigenvector. The transformation X=TZ is applied to equations 3 and 5 and results in a block diagonal form in terms of modal coordinates, Z, as

$$\dot{Z} = [\, T^{-1}(A-B_1K-LC)T]\, Z+(T^{-1}L)Y$$

$$u = (-KT)Z \qquad (A4)$$

References

1. Doggett, R. V.; and Townsend, J. L.: Flutter Suppression by Active Controls and Its Benefits. Proceedings of the SCAR Conference, NASA CP-001, 1976.

2. Newsom, J. R.: A Method for Obtaining Practical Flutter Suppression Control Laws Using Results of Optimal Control Theory. NASA TP-1471, 1979.

3. Mukhopadhyay, V.; Newsom, J. R.; and Abel, I.: A Method for Obtaining Reduced-Order Control Laws for High-Order Systems Using Optimization Techniques. NASA TP-1876, 1981.

4. Mahesh, J. K.; Stone, C. R.; Garrard, W. L.; Dunn, H. J.: Control Law Synthesis for Flutter Suppression Using Linear Quadratic Guassian Theory. J. Guidance and Control, Vol. 4, No. 4, July-August 1981, pp. 415-422.

5. Gangsaas, D.; and Ly, U.: Application of a Modified Linear Quadratic Gaussian Design to Active Control of a Transport Airplane. AIAA Paper 79-1746, August 1979.

6. Hwang, C.; and Pi, W. S.: Application of Optimal Control Techniques to Aircraft Flutter Suppression and Load Alleviation. AIAA 23rd Structures, Structural Dynamics and Materials Conference, New Orleans, Louisiana, May 1982.

7. Newsom, J. R.; Abel, I.; and Dunn, H. J.: Application of Two Design Methods for Active Flutter Suppression and Wind-Tunnel Test Results. NASA TP-1653, May 1980.

8. Abel, Irving; Perry, Boyd III; and Newsom, Jerry R.: Comparison of Analytical and Wind-Tunnel Results for Flutter and Gust Response of a Transport Wing With Active Controls. NASA TP-2010, 1982.

9. Johnson, E. H.; Hwang, C.; Pi, W. S.; Kesler, D. F.; and Joshi, D. S.: Test Demonstration of Digital Control of Wing/Store Flutter. AIAA 23rd Structures, Structural Dynamics and Materials Conference, New Orleans, Louisiana, May 1982.

10. Roger, K. L.; Hodges, G. E.; and Felt, L.: Active Flutter Suppression--A Flight Demonstration. J. of Aircraft, pp. 551-556, June 1975.

11. Murrow, H. N.; and Eckstrom, C. V.: Drones for Structural Testing (DAST) - A Status Report. J. Aircraft, vol. 16, no. 8, Aug. 1979, pp.521-526.

12. Edwards, J. W.: Flight Test Results of an Active Flutter Suppression System Installed on a Remotely Piloted Research Vehicle. AIAA Paper No. 81-0655, April 1981.

13. Newsom, J. R.; and Pototzky, A. S.: Comparison of Analysis and Flight Test Data for a Drone Aircraft with Active Flutter Suppression. AIAA Paper No. 81-0640, April 1981.

14. Bennett, R. M.; and Abel, I.: Application of a Flight Test and Data Analysis Technique to Flutter of a Drone Aircraft. AIAA Paper No. 81-0652, April 1981.

15. Eckstrom, C. V.; and Spain, C. V.: Design Considerations and Experiences in the Use of Composite Material for an Aeroelastic Research Wing. AIAA Paper No. 82-0678, May 1982.

16. Whetstone, W. D.: EISI-EAL: Engineering Analysis Language. Proceedings of the Second Conference on Computing in Civil Engineering, American Soc. Civil Eng., 1980, pp. 276-285.

17. Peele, E. L.; and Adams, W. M., Jr.: A Digital Program for Calculating the Interaction Between Flexible Structures, Unsteady Aerodynamics, and Active Controls. NASA TM-80040, 1979.

18. Doyle, J. C.; and Stein, G.: Robustness With Observers. IEEE Trans. Autom. Control, Vol. AC-24, No. 4, Aug. 1979, pp. 607-611.

19. Kwakernaak, Huibert; and Sivan, Raphael:
Linear Optimal Control Systems. John Wiley
& Sons, Inc., c. 1972.

Table 1 EAL computed natural frequencies (Hz) of the initial structure

MODE	SYMMETRIC	ANTISYMMETRIC
1	10.1	12.3
2	17.0	21.1
3	30.3	32.1
4	36.4	32.7
5	39.5	35.2
6	44.0	43.4
7	49.5	45.5
8	70.6	54.2
9	74.9	71.6
10	79.7	74.9

Table 2 EAL computed and GVT natural frequencies (Hz) of the updated structure

MODE	EMPTY FUEL				MID FUEL		FULL FUEL	
	SYMMETRIC	GVT DATA	ANTISYMMETRIC	GVT DATA	SYMMETRIC	ANTISYMMETRIC	SYMMETRIC	ANTISYMMETRIC
1	9.1	9.3	13.2	13.6	9.1	13.2	9.1	11.7
2	15.8	16.1	18.2	18.2	15.1	17.5	14.3	17.0
3	30.9	30.3	29.0	28.5	30.8	29.0	30.7	29.0
4	37.6	-	32.7	32.7	37.4	32.7	34.9	31.4
5	40.3	-	34.7	-	40.2	34.5	40.2	33.9
6	46.3	-	43.3	-	46.3	43.3	46.3	43.1
7	49.4	-	46.6	-	49.4	46.6	49.4	45.3
8	62.8	-	50.8	-	61.7	50.5	59.8	49.4
9	76.1	-	68.5	-	74.4	68.4	72.6	67.6
10	86.2	-	75.2	-	85.8	74.4	79.7	74.2

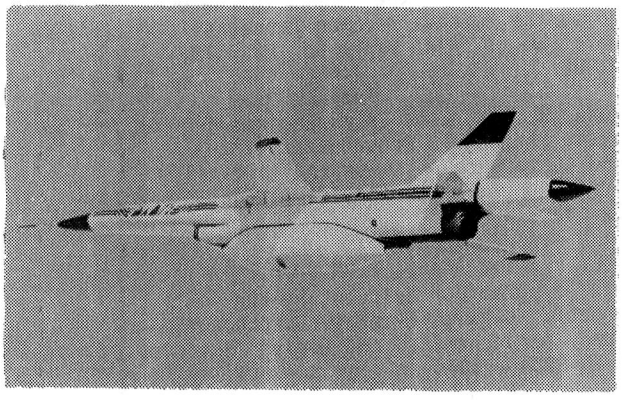

Fig. 1 DAST vehicle.

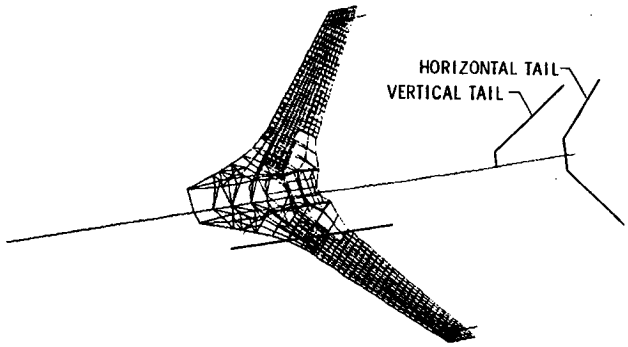

(a) Finite element, structural model of DAST ARW-1R

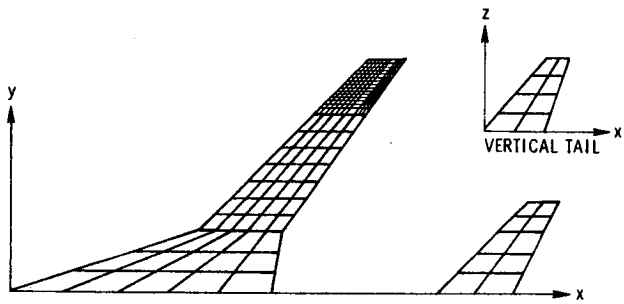

(b) Doublet lattice box layout used in modeling the unsteady aerodynamics

Fig. 2 Structural and aerodynamic models.

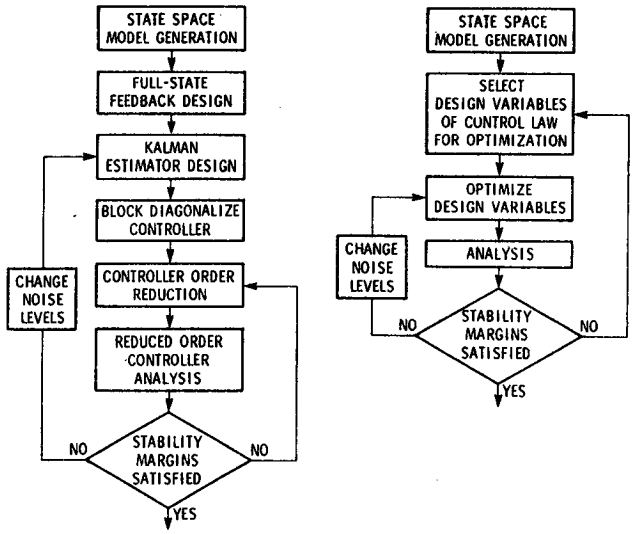

(a) Modified linear quadratic Gaussian approach

(b) Numerical optimization approach

Fig. 4 Flow charts of optimal control law synthesis approaches.

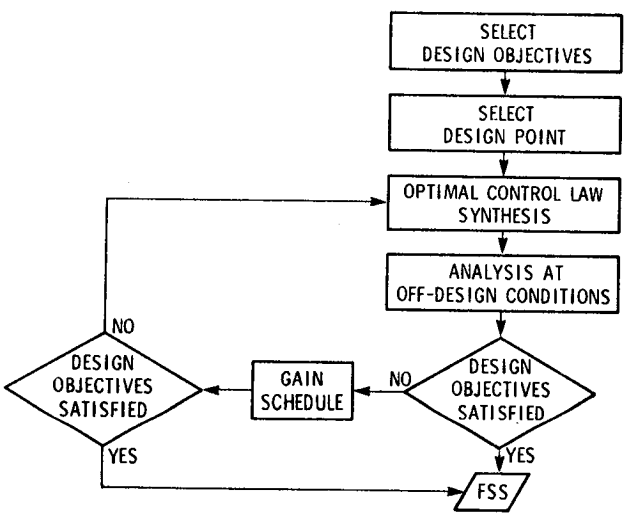

Fig. 3 Flow chart of overall control law design process.

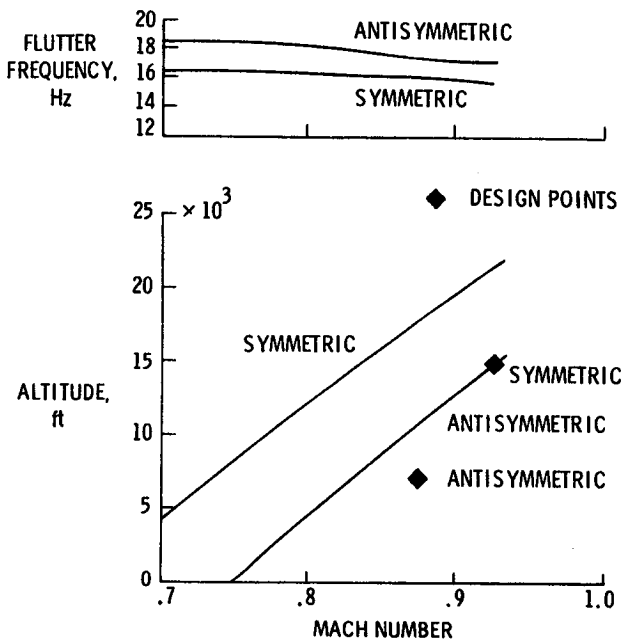

Fig. 5 Predicted FSS-off flutter boundaries and frequencies.

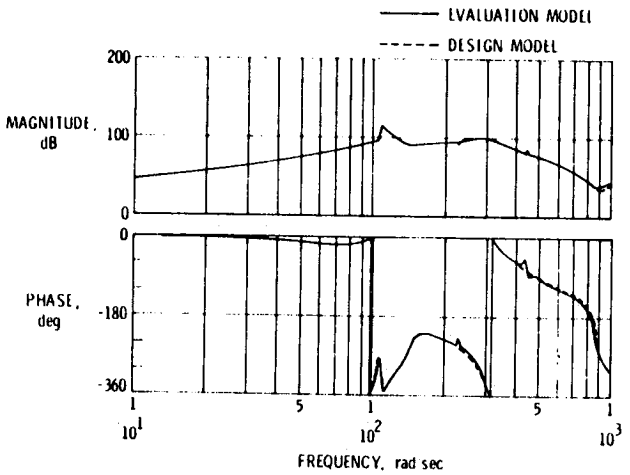

Fig. 6 Bode plot of the open-loop frequency response function $\ddot{z}_w/\delta_c$ for both the evaluation and design models. (symmetric design point; M = 0.925 at 15,000 feet)

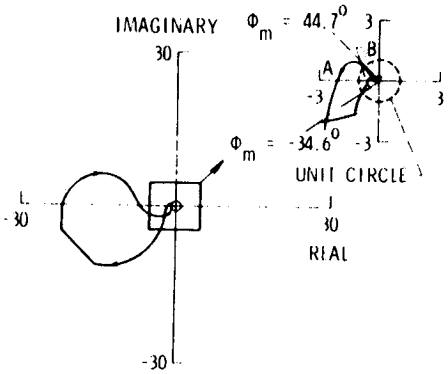

POINTS	GAIN MARGINS
A	-6.0 dB
B	4.7 dB

(a) Symmetric, M = 0.925 at 15,000 feet

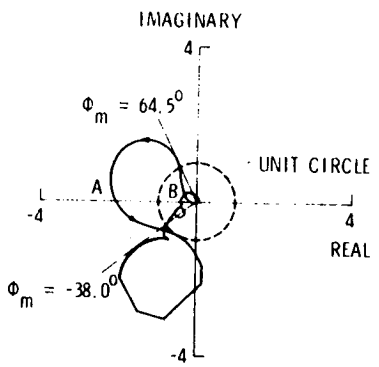

POINTS	GAIN MARGINS
A	-6.3 dB
B	8.3 dB

(b) Antisymmetric, M = 0.875 at 7,000 feet

Fig. 7 Nyquist plots at design points.

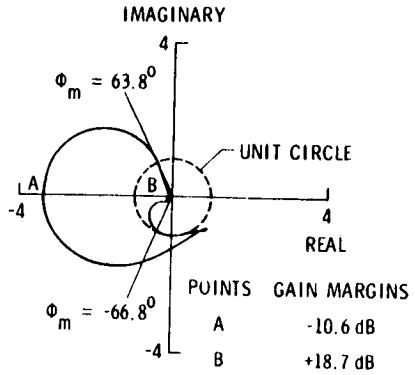

POINTS	GAIN MARGINS
A	-10.6 dB
B	+18.7 dB

(a) Symmetric, M = 0.85 at 15,000 feet

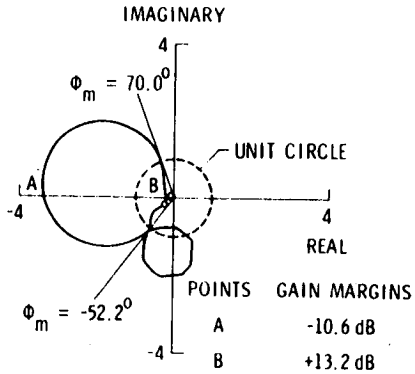

POINTS	GAIN MARGINS
A	-10.6 dB
B	+13.2 dB

(b) Antisymmetric, M = 0.85 at 7,000 feet

Fig. 8 Nyquist plots near FSS-off flutter boundary.

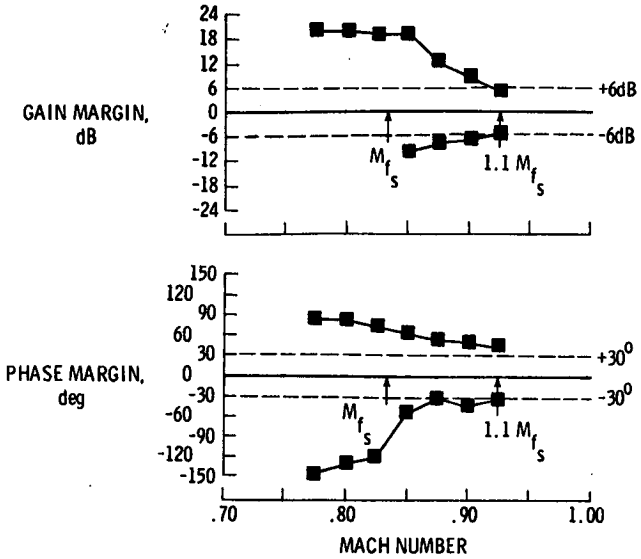

(a) Symmetric, 15,000 feet

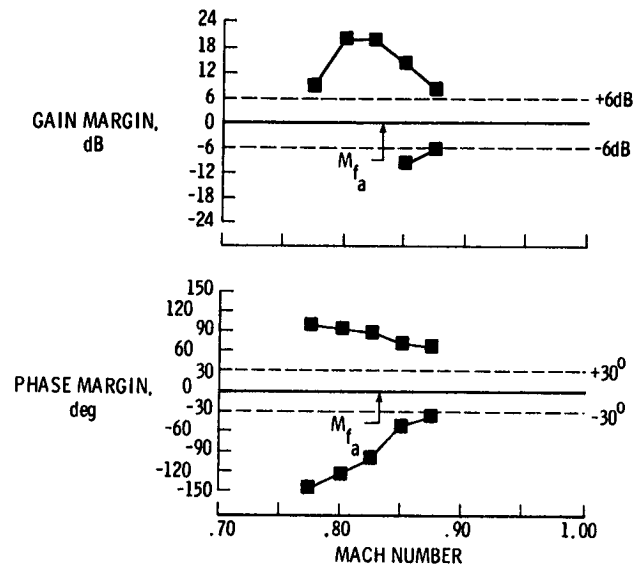

(b) Antisymmetric, 7000 feet

Fig. 9 Stability margins as a function of Mach Number.

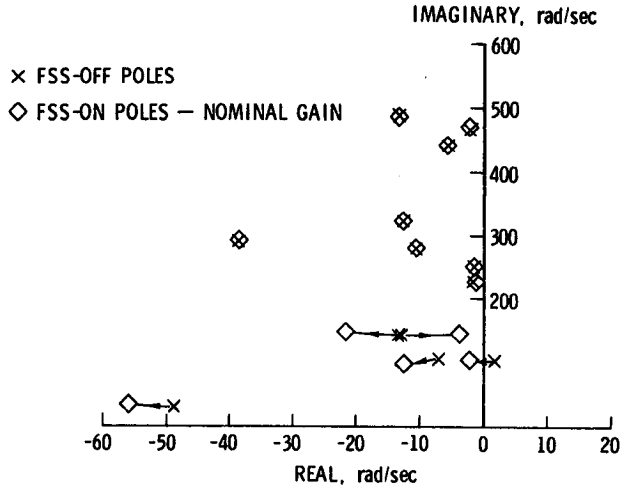

(a) Symmetric, M = 0.85, 15,000 feet

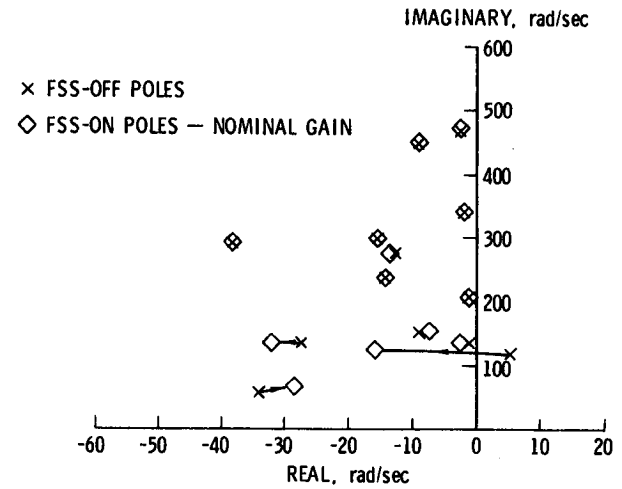

(b) Antisymmetric, M = 0.85, 7,000 feet

Fig. 10 Gain root locus with initial control law near FSS-off flutter boundary (arrows indicate increasing gain).

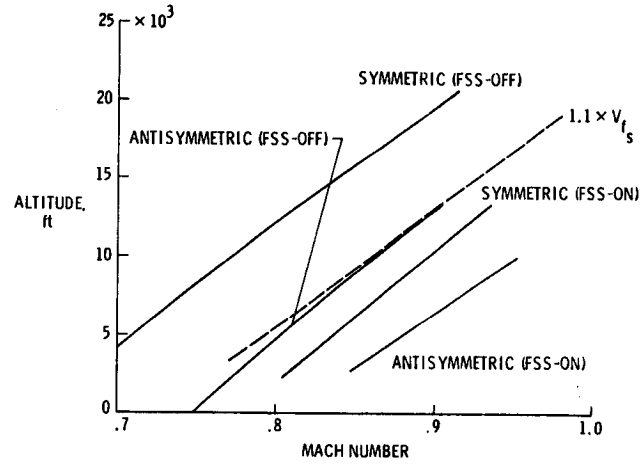

Fig. 11 Flutter boundary with the control law defined by eq. 7 and gain schedule of eq. 9.

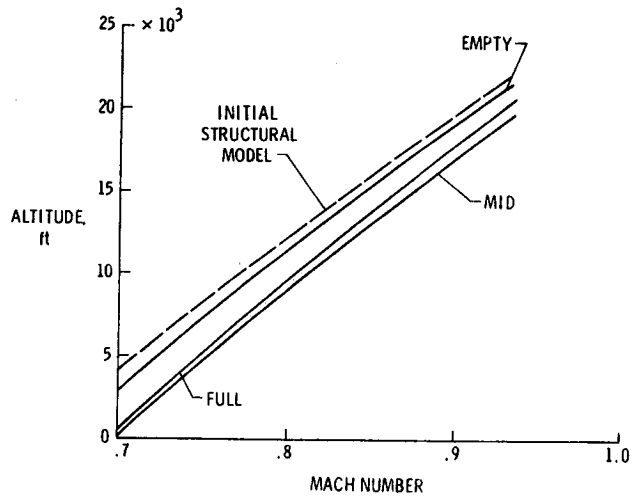

(a) Symmetric

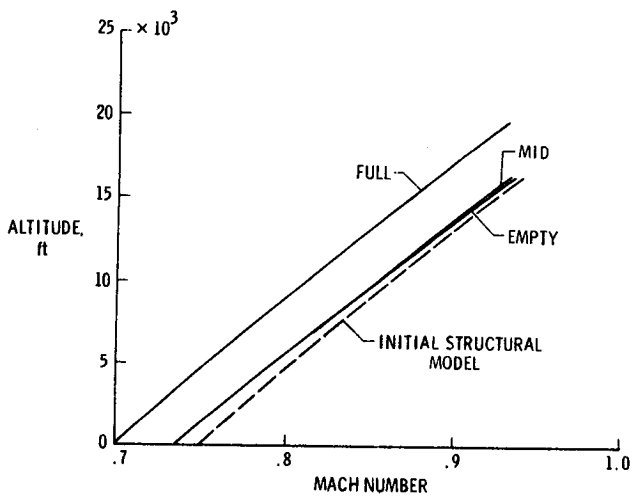

(b) Antisymmetric

Fig. 12 FSS-off flutter boundary of the updated ARW-1R model at various fuel weight conditions.

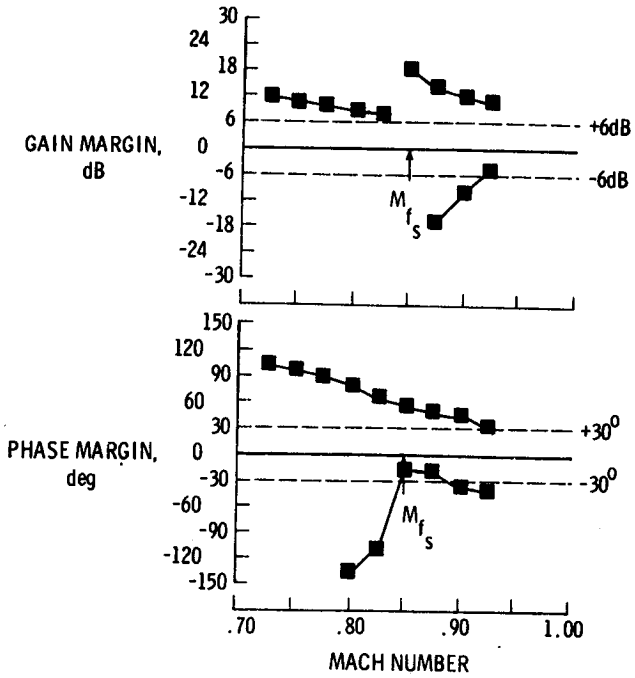

(a) Symmetric

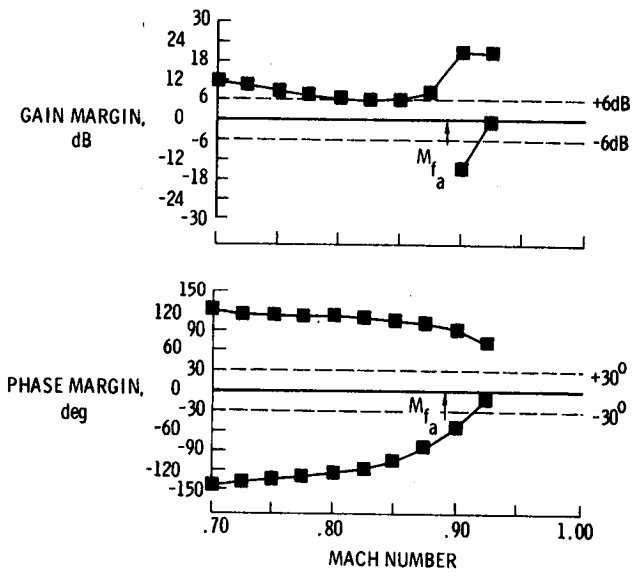

(b) Antisymmetric

Fig. 13 Stability margins as a function of Mach Number at 13,000 feet.

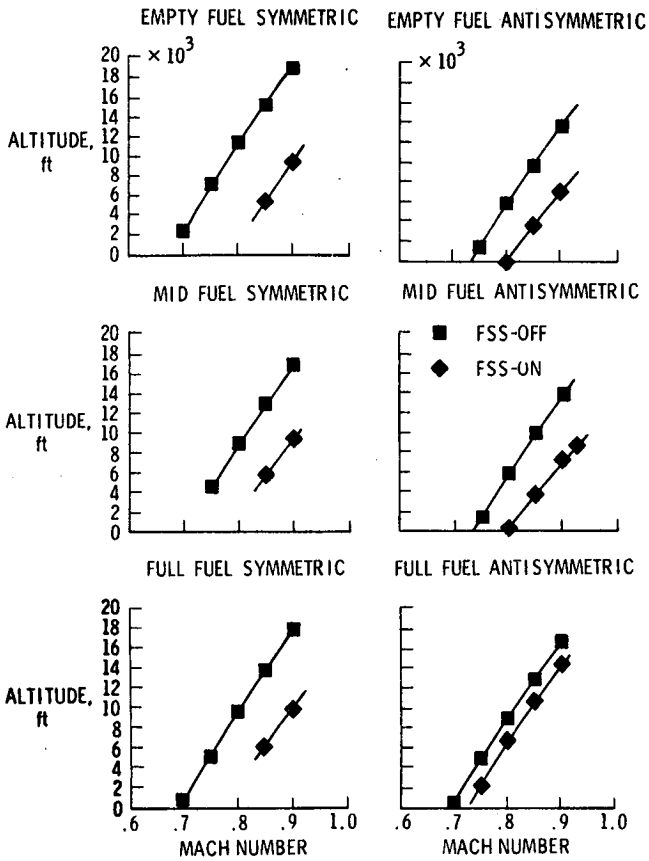

Fig. 14 Flutter boundaries with the updated ARW-1R model at various weight conditions using gain scheduled control law.

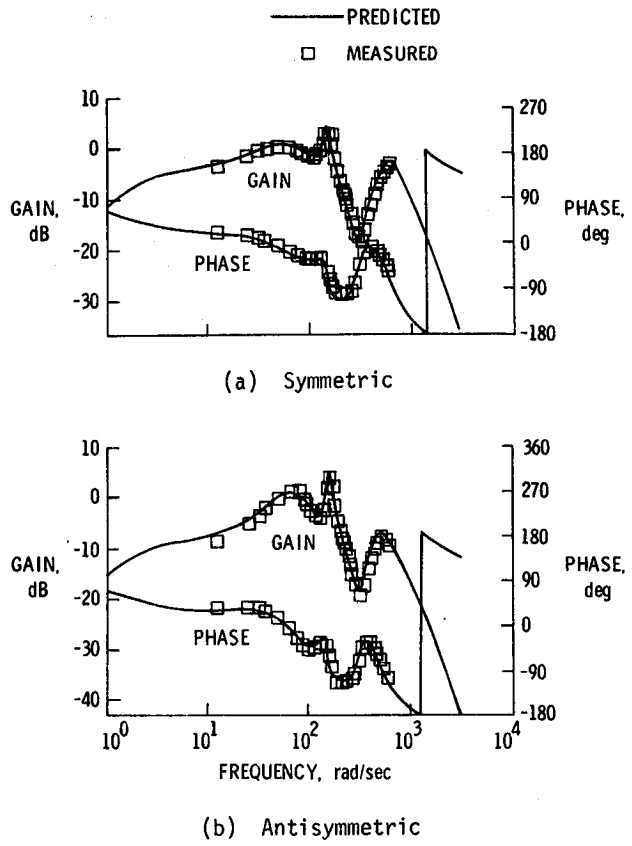

Fig. 16 Comparison of predicted and measured FSS frequency response.

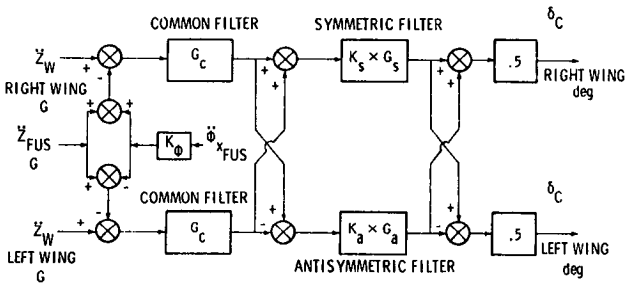

Fig. 15 FSS block diagram.

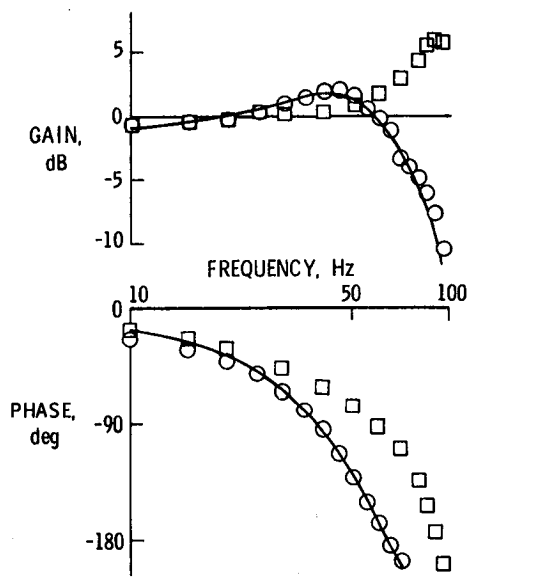

Fig. 17 Bode plot of actuator frequency response function.

1. Report No.	2. Government Accession No.	3. Recipient's Catalog No.
NASA TM 84642		

4. Title and Subtitle	5. Report Date
DESIGN OF THE FLUTTER SUPPRESSION SYSTEM FOR DAST ARW-1R - A STATUS REPORT	March 1983
	6. Performing Organization Code 505-33-43-08
7. Author(s) Jerry R. Newsom*, Anthony S. Pototzky**, and Irving Abel*	8. Performing Organization Report No.
	10. Work Unit No.
9. Performing Organization Name and Address NASA Langley Research Center Hampton, VA 23665	11. Contract or Grant No.
	13. Type of Report and Period Covered Technical Memorandum
12. Sponsoring Agency Name and Address National Aeronautics and Space Administration Washington, DC 20546	14. Sponsoring Agency Code

15. Supplementary Notes *Langley Research Center, **Kentron International, Inc.
Presented at AIAA/ASME/ASCE/AHS 24th Structures, Structural Dynamics and Materials Conference, Lake Tahoe, Nevada, May 2-4, 1983. AIAA # 83-0990

16. Abstract

This paper describes the design of the flutter suppression system for a remotely-piloted research vehicle. The modeling of the aeroelastic system, the methodology used to synthesize the control law, the analytical results used to evaluate the control law performance, and ground testing of the flutter suppression system onboard the aircraft are discussed. The major emphasis is on the use of optimal control techniques employed during the synthesis of the control law.

17. Key Words (Suggested by Author(s))	18. Distribution Statement
flutter, active controls	Unclassified - Unlimited Subject Category - 63

19. Security Classif. (of this report)	20. Security Classif. (of this page)	21. No. of Pages	22. Price
Unclassified	Unclassified	14	A02

For sale by the National Technical Information Service, Springfield, Virginia 22161